PROCEEDINGS OF SPIE

SPIEDigitalLibrary.org/conference-proceedings-of-spie

Structural analysis and testing of silicon x-ray mirror modules

Peter M. Solly, Michael Biskach, Joseph A. Bonafede, Kai-Wing Chan, James Mazzarella, et al.

Peter M. Solly, Michael Biskach, Joseph A. Bonafede, Kai-Wing Chan, James Mazzarella, Ryan McClelland, Timo T. Saha, William W. Zhang, "Structural analysis and testing of silicon x-ray mirror modules," Proc. SPIE 11119, Optics for EUV, X-Ray, and Gamma-Ray Astronomy IX, 111190B (9 September 2019); doi: 10.1117/12.2530338

SPIE.

Event: SPIE Optical Engineering + Applications, 2019, San Diego, California, United States

Structural Analysis and Testing of Silicon X-Ray Mirror Modules

Peter M. Solly*[a,c], Michael Biskach[a,c], Joseph A. Bonafede[a], Kai-Wing Chan[b,c], James Mazzarella[a,c], Ryan McClelland[c], Timo T. Saha[c], William W. Zhang[c]

[a]KBR Space Engineering Division, 7701 Greenbelt Road, Suite 400, Greenbelt, Maryland 20770, USA
[b]Center for Research and Exploration in Space Science and Technology & University of Maryland, Baltimore County, Baltimore, MD 21250, USA
[c]NASA Goddard Space Flight Center (GSFC), Greenbelt, MD USA 20771, USA

ABSTRACT

The fundamental developmental issue facing the next generation of X-ray astronomical telescopes is the manufacturability, assembly, and structural robustness of the grazing incidence optics. Combining the high angular resolution requirements with large effective areas and physical launch vehicle restrictions leads to very thin shelled optics that must remain very stable. Meeting these stability requirements while also surviving launch and space environments presents a significant engineering challenge. Over the last few years, the Next Generation X-ray Optics (NGXO) team at NASA Goddard has been developing thin segmented silicon optics that are assembled into both modules and meta-shells, which show great promise in meeting these challenges. This paper summarizes the analytical approaches, as well as the environmental tests, used to assess such assemblies. Many parameters in the design space of the assembly have been assessed and optimized using Finite Element (FE) models and ray trace algorithms. The results of these analyses have helped shape reasonable and justifiable error budgets, as well as guide the team's decision making in both near and long term processes. The structural integrity of an assembly has been assessed both with testing and FE models. Preliminary strength testing has been conducted on the basic components used in the assembly.

Keywords: silicon mirrors, meta-shell, module, mirror assembly, X-ray optics, structural analysis, optimization, finite element model

*Peter M Solly, peter.m.solly@nasa.gov

1. INTRODUCTION

Silicon X-ray optics are a relatively new and exciting possible technology paradigm for future X-ray telescopes. Over the last few years, substantial progress has been made in developing facets of this technology [1], starting with the mass production of individual mirrors thru the concept for the integration of a complete optical assembly.

1.1 Four Point Mount and Mirror Dimensions

Individual mirror substrates, Figure 1-1, have been produced to exceptional sub-arcsecond quality [2] using a precision polishing process that is compatible with mass production [3]. The baseline size of the mirrors is 100mm by 100mm, with a thickness of 0.5mm. The current manufacturing paradigm utilizes 150mm square blocks, and requires removal of the outer border due to edge effects from the polishing process. These dimensions can be adjusted if the optical prescription requires it due to other considerations such as diffraction or off-axis Point Spread Function (PSF). The mirror thickness is a more open variable, as the polishing process has been demonstrated for thicknesses from 0.4mm to 1.2mm. The thickness can be modified to meet competing requirements of rocket payload capacity, mirror effective area, and survivability. Much of the mirror level analysis in this paper therefore examines a range of mirror thickness, while the length and width are generally treated as a fixed variable.

One of the core principles of silicon meta-shell optics is the kinematic nature of a 4 point mount of a curved substrate. The four posts have precisely lapped conical tips, to produce a near perfect radial point constraint at the post location. The four point constraints together constrain the mirror in the X (radial de-center), Y (azimuthal de-center), RX (Yaw),

Optics for EUV, X-Ray, and Gamma-Ray Astronomy IX, edited by Stephen L. O'Dell, Giovanni Pareschi, Proc. of SPIE Vol. 11119, 111190B · © 2019 SPIE · CCC code: 0277-786X/19/$21 · doi: 10.1117/12.2530338

and RY (Pitch) directions. The Z (de-focus) and RZ (roll) directions can then be constrained using two point contacts (one on the side, one at the bottom) on the edges of the mirror using alignment pins. This minimally constrained system allows for precise alignment of the mirrors by virtue of the stress free state (the only force acting on the mirror is gravity, which can be accurately predicted) and repeatable placement capability [4].

Figure 1-1 A representative silicon X-ray optic, 100mm by 100mm by 0.5mm

1.2 Modules

The mirrors can be assembled into modules as stack like structures using a thicker silicon plate as a mounting base structure. Modules require meeting the additional challenges of co-aligning multiple pairs of mirrors to the same focal point and accounting for additional possible integration errors such as gravity sag of the mounting plate. Our group has generated conceptual designs for two types of modules, one where the mounting plate is used as a baseplate for a single overhanging stack, as seen in Figure 1-2, and another where the mounting plate is in effect a mid-plate holding stacks of mirrors on both sides, a concept that produces more effective mirror area for the blocked area of a given mounting plate.

Figure 1-2 A module concept of multiple silicon X-ray mirror pairs

1.3 Meta-shells

Meta-shells can consist of either assemblies of modules mounted to silicon rings, or an interlocking set of individual mirrors mounted directly to a large structural cylinder, multiple of which are shown in Figure 1-3. An assembly of modules adds a layer of modularity to the design and assembly process, which has significant advantages in terms of schedule and testing, as well as redundancy and the ability to generate flight spares in case of an error or incident during integration. An interlocked meta-shell has the advantage of reduced integration steps and a simple direct alignment and integration procedure.

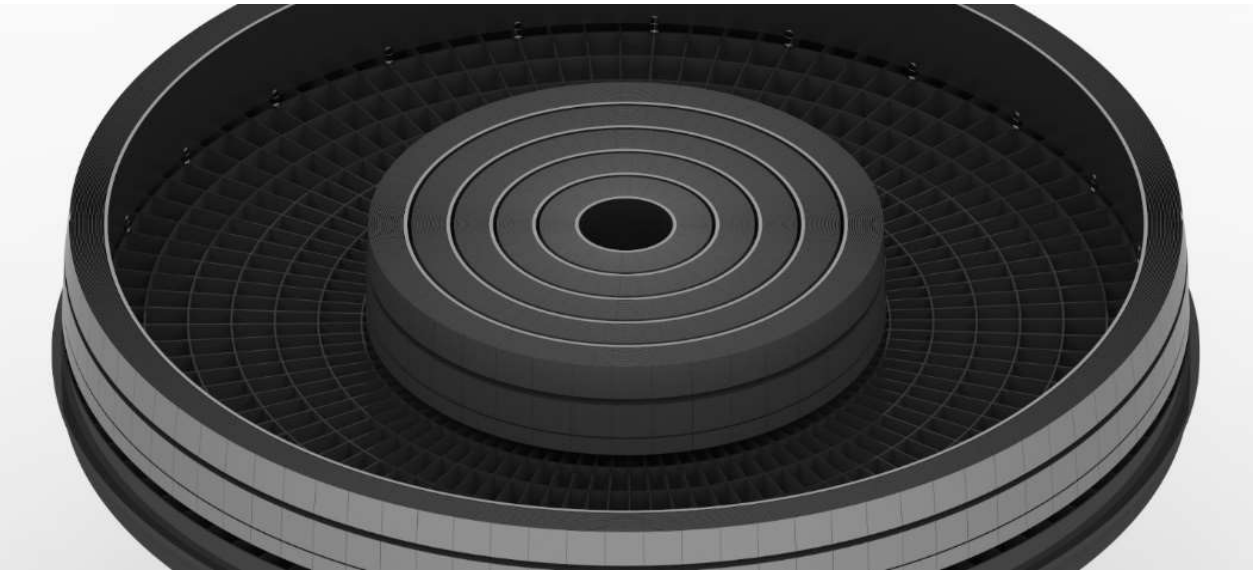

Figure 1-3 A flight like assembly of multiple meta-shells using silicon X-ray optics

2. STRUCTURAL ANALYSIS AND OPTIMIZATION

Key to maximizing the performance of an X-ray telescope using silicon optics mounted at 4 points is to optimize all parameters at the individual mirror level. Much of the analytical work over the last few years has been focused on formulating the ideal process at this level, optimizing dimensions and materials while understanding the impacts of various steps in the process.

With many assembly parameters such as post location optimized at the mirror level, the main concern at the module level is reducing the effects of additional error sources in the assembly process while designing a viable structural element suited for spaceflight.

Similar to the module level work, the meta-shell work builds upon the optimized parameters developed at the mirror level, and is more focused on top level effects. Again the goal is minimizing additional forms of distortion for the mirror and designing a robust structure. Additionally, the meta-shell level requires additional examination of mission level effects such as on orbit thermal.

2.1 Post Spacing Optimization

One of the first questions posed by the four point mount is where precisely to locate the contact points on the mirror. An initial assumption may be to locate the points equidistant (25%) along each edge, however this does not minimize the mirror deflection and the bending moment that gets frozen in when the adhesive under the mirror cures and changes the boundary condition at each point from 1 Degree of Freedom (DOF) to 6 DOF (the bending moment then leads to stress/deformation when gravity is removed in space). In beam theory, the Bessel/Airy points are well defined and locate the support points at 22.0% and 21.1% from the edges, respectively. The Airy points define the locations that generate no slope at the edge of the beams, but for minimizing frozen in distortion a more logical condition would be to determine locations with no slope at the support points. A slight change to the Airy point derivation can then be set up, which leads to support points at 22.5% from the edge (55.05mm spacing between points of a 100mm beam). For conical, 2D silicon mirrors, the mechanics are not as easily derived, so a detailed trade study using FE models was performed.

The metric used for optimization is the “frozen in” distortion of the mirror mount. This is calculated by analyzing the deflection of a mirror under two boundary conditions: (1) simply supported (1 DOF) at each post location under gravity, and (2) fully fixed (6 DOF) at each post location under negative gravity (release). The net difference between these two cases is considered the frozen in distortion that will remain after a mirror is precisely located/bonded under gravity, and subsequently released to 0G in space. This does not minimize distortion seen under gravity during integration, which could be optimized similarly and result in different locations. To run thru the tradespace, both a coarse (25 node by 25 node) and fine (101 by 101 node) model was generated for a silicon mirror pair with intersection

diameter of 312mm, axial length of 100mm, azimuthal span of 30 degrees, and focal length of 8.4m. The coarse model is used to analyzed the full set of possible symmetric mounting points (144 cases), while the fine model is used to gain a clearer picture around the quarter points (400 cases) as shown in Figure 2-1. Multiple mirror thickness values are run for both models to capture the effects of mirror stiffness on the results. Python scripts are used to generate the constraint sets and ray trace the resulting data sets. The resulting frozen in distortion by mounting point can be seen in Figure 2-2, and summarized in Table 2-1.

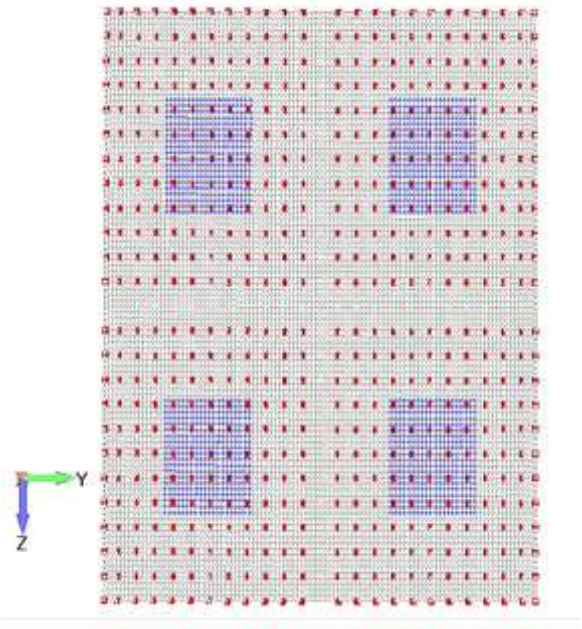

Figure 2-1 Mirror with mounting points for coarse (red) and fine (blue) highlighted

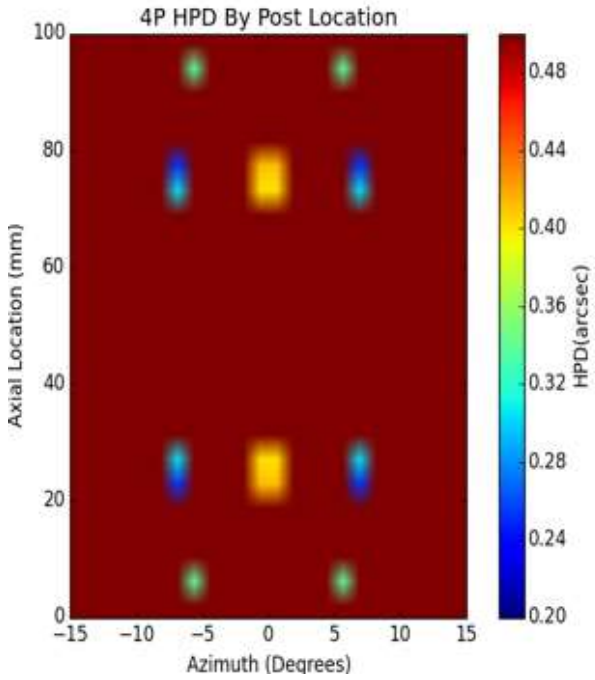

Figure 2-2 Frozen in distortion HPD based on mounting locations (coarse mode, 0.5mm thickness)

Table 2-1 Frozen In optimization results summary

Model	Mirror Thickness (mm)	Minimum HPD (arc-sec)	Post Location	
			Azimuthal Span (deg)	Axial Span (mm)
Coarse (25 node mirrors)	0.50	0.26	15	58
	0.75	0.15	15	58
	1.00	0.11	2.5	50
	1.25	0.07	2.5	42
	1.50	0.04	2.5	50
Fine (101 node	0.50	0.14	15	54
	1.00	0.05	14.4	56

The results along the quarter point azimuths are of particular interest, since developing an interlocked meta-shell would likely necessitate keeping the posts lined up, which can only be achieved at the quarter points. With that assumption, the plot for Half Power Diameter (HPD) by axial spacing can be seen in Figure 2-3.

(a)

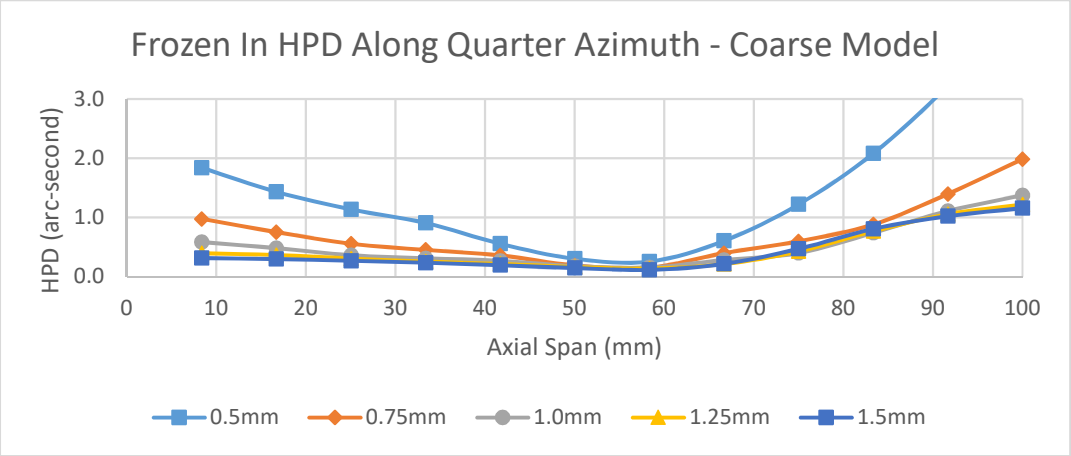

(b)

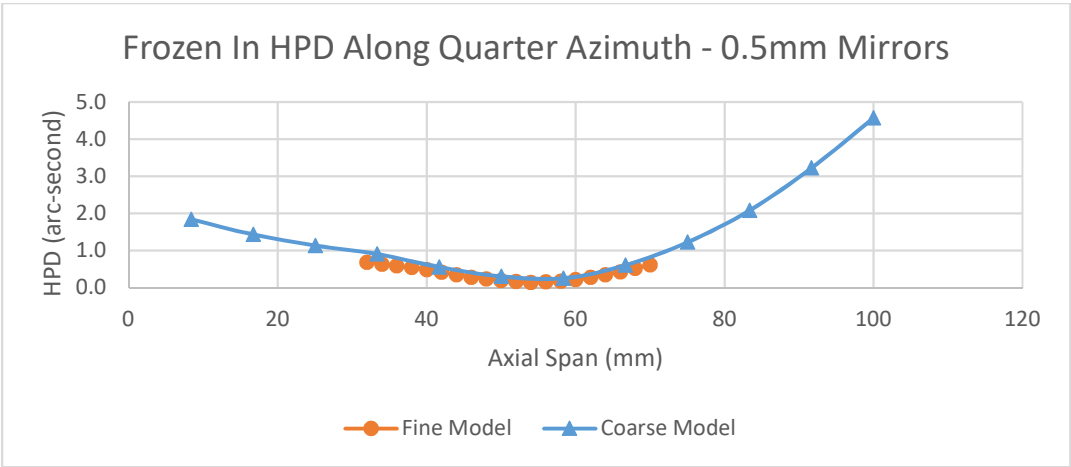

(c)

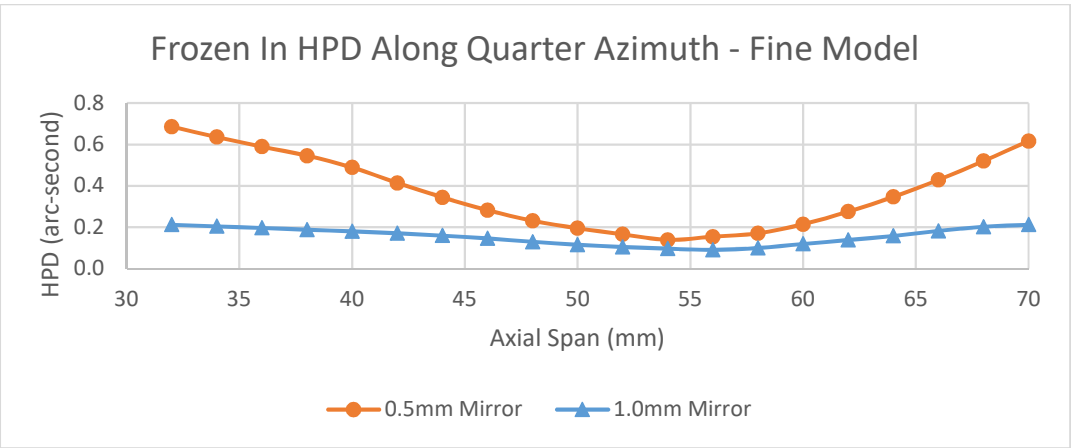

Figure 2-3 Plots of resulting HPD data along quarter point azimuths for (a)coarse models, (b)0.5mm mirrors from both models, (c)fine models

The frozen in distortion for mirror pairs mounted on the quarter azimuths appears to reach its minimum between 54mm and 56mm axial spacing. This result agrees well with the calculated locations for a beam with zero slope at the mounting points (aforementioned 55.05mm), and is very close to the 56mm spacing that has been used in all alignment and mounting efforts to date [5].

2.2 Post Height Sensitivity

The kinematic nature of the four point mount allows for fine tuning of mirror alignment using a precision polishing process to adjust the height of the four spacers. The precision of this machining process is an ongoing engineering development. To capture the relationship between this accuracy and the resulting mirror alignment error that can be flowed into a full error budget, a detailed statistical sensitivity study was performed using analytical methods.

A simple mirror pair model of finely meshed elements was used, identical to that used in section 2.1, and minimally constrained (1 DOF at four post locations, along with additional alignment pin stops for axial translation and roll DOF). For post height machining, the machining tolerance is defined as the 3σ value of a normal distribution. This assumes that any bias is accounted for in the calibration and development of the polishing process. For various machine tolerance values, 100 cases of post height errors are generated as enforced displacements at the mount points in the kinematic model. Each case requires 8 displacements (4 mount points on primary/secondary), hence 800 randomly generated values. A coarser (37 node by 37 node) model was also setup to gain more clarity at a specific tolerance, in this case 20nm, with 1000 cases (8000 displacements). A summary of the generated errors for those cases is shown in Figure 2-4.

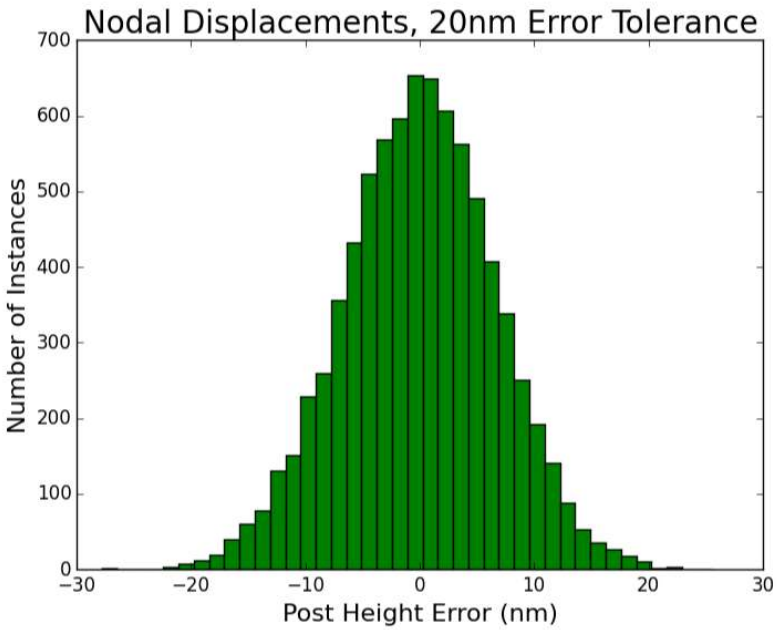

Figure 2-4 Random distribution of post height errors

The error cases are then processed with FEMAP/NASTRAN, and resulting mirror displacements ray traced to determine the effect on mirror alignment. The results indicate a strong linear relationship (Figure 2-5) between the prescribed machining error tolerance ($T_{3\sigma}$) and resulting image quality error (HPD_{avg}):

$$HPD_{avg} = 0.0058 * T_{3\sigma}$$

For an estimated error tolerance of 20nm, the average image quality error was 0.117 arc-seconds HPD. The distribution of errors (Figure 2-6) is also shown to be right tailed, as the median image quality error was lower at 0.097 arc-seconds. It should be noted that outlier cases in the distribution at the edge of the right tail would likely be noticeable in the alignment process and could be reduced with a 2nd pass of height adjustment prior to mirror bonding.

Figure 2-5 Mirror figure error as a function of post height tolerance

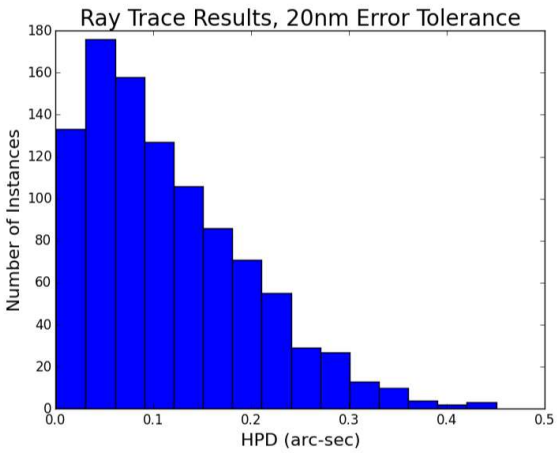

Figure 2-6 Distribution of mirror figure error results from randomly distributed post height errors

The results were found to be relatively independent of mirror radii, span, and thickness, indicating that this relationship should hold for various possible mirror prescriptions.

2.3 Adhesive Curing Analysis

Epoxy curing/shrinkage between the mirror surface and crowned posts can generate a stress that significantly distorts the mirror. To gauge the possible effects, a detailed FE model was generated of a 312mm diameter mirror pair (see section 2.1) mounted to a solid silicon block that is kinematically mounted, all meshed with 3D anisotropic elements for the silicon, see Figure 2-7.

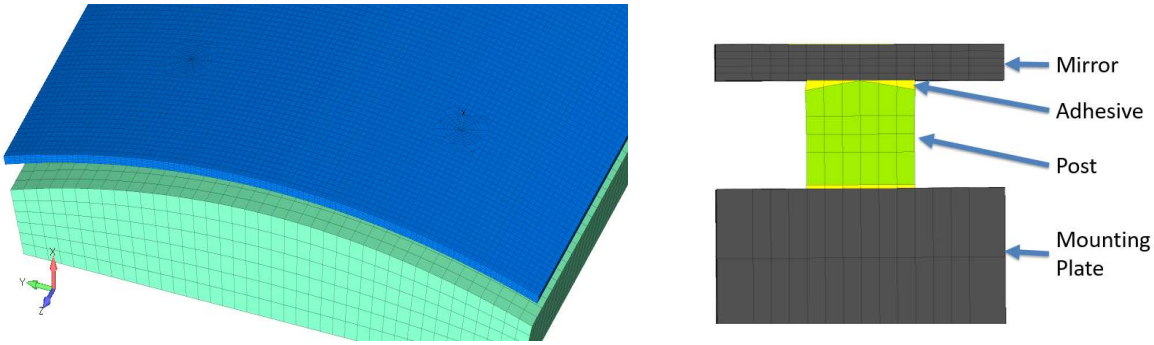

(a) (b)

Figure 2-7 (a) FE Model used for study of bond distortion (b) close up of post/adhesive

Five variables were examined parametrically to determine their general effect on cure distortion:

- Post diameter (1mm to 6mm)
- Mirror thickness (0.4mm to 1.0mm)
- Epoxy cure strain (.005% to 1%)
- Post material stiffness (silicon to steel)
- Post crown cone angle (2 degrees to 10 degrees)

The primary concern was the combined effects of mirror thickness and post diameter. Mirrors have generally been manufactured anywhere between 0.4mm and 1.0mm, with 0.5mm thickness being a common assumption for full telescope designs. To date, posts have been manufactured at 3mm and 4mm diameters, both steel and silicon. Models

were setup with varying post size and mirror thicknesses, all with: silicon posts, 186ppm strain (value correlated to Hysol 9309 strain tests on a mirror), and post crown cone angle of 10 degrees (extra conservative, posts are currently fabricated with 4 degree crown). The results from these models is summarized in Table 2-2.

Table 2-2 Bond distortion by mirror thickness and post diameter

Cure Distortion HPD (arc-sec)					
Post Diameter (mm)	Mirror Thickness (mm)				
	1	0.8	0.6	0.5	0.4
1.0	0.02	0.03	0.05	0.05	0.06
2.0	0.1	0.14	0.19	0.24	0.36
3.0	0.23	0.36	0.58	0.78	0.89
4.0	0.47	0.78	1.29	1.53	1.63
5.0	0.83	1.33	2.13	2.37	2.49
6.0	1.25	2.14	2.99	3.32	3.42

The data shows a clear second order relationship with post diameter (linear with post surface area), and a semi-linear relationship with mirror thickness, with a steeper transition between 0.5mm and 0.8mm, shown in Figure 2-8 and Figure 2-9.

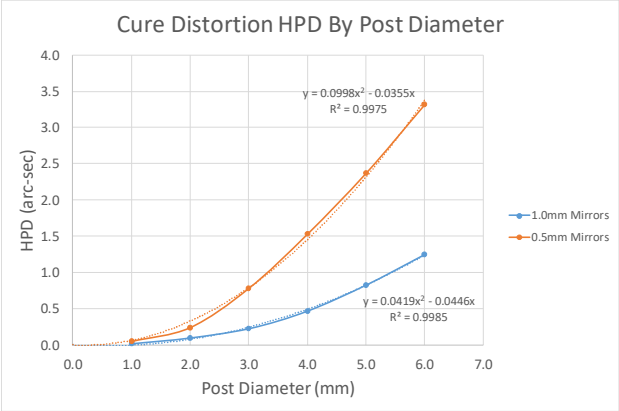

Figure 2-8 Bond distortion relationship with post diameter

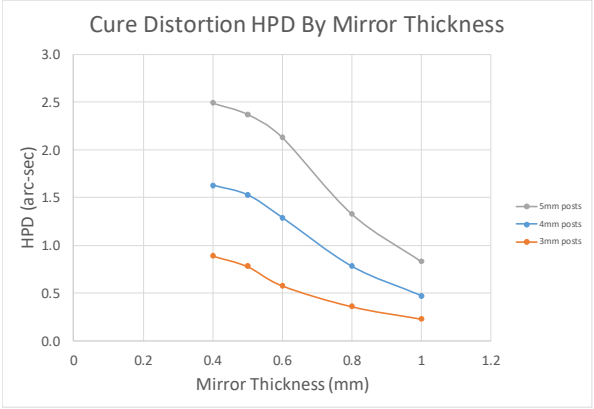

Figure 2-9 Bond distortion relationship with mirror thickness

Other possible variables were also examined. The applied cure strain was found to have a pure linear effect with mirror distortion, while post stiffness was found to have negligible effect in the relevant range between 90 and 210 GPa. The effects of cone angle were assessed using a separate model of a flat plate, with a finer mesh at the posts (all 4mm). Data was then generated for both 0.5mm thick plates and 1.0mm thick plates. The resulting surface RMS distortion is used as the metric, and shows good correlation with the square root of the cone angle, FE model and results are shown in Figure 2-10.

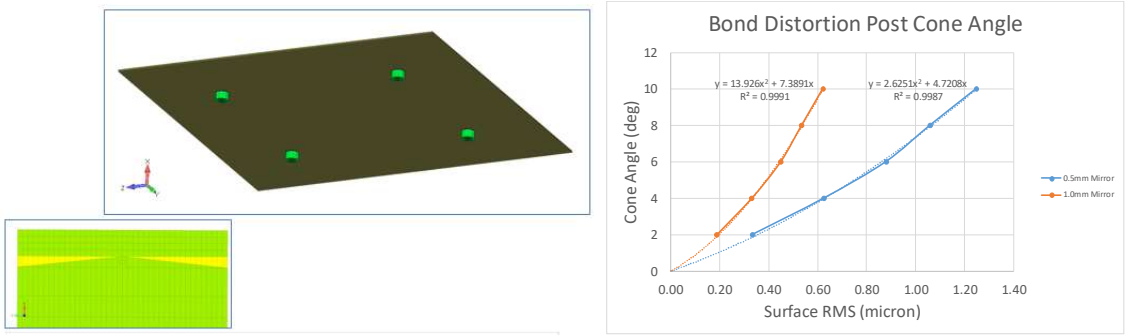

Figure 2-10 Flat plate FE model and bond distortion relationship with post crown cone angle

2.4 Shell Thickness

The silicon mirrors are mounted to a thicker, non-polished piece of silicon, denoted as the mounting plate (for modules) or structural shell (for meta-shells). In either case, the thickness of the mounting plate should be minimized, as the thickness reduces the overall efficiency of the X-ray telescope and increases mass. The main considerations for increasing the thickness are to maintain image performance and stiffness. For a module mounting plate, stiffness was found to be sufficient even for thin shells; the driving parameter was mirror performance. A simple trade study was conducted by ray tracing the first pair in a 16 pair stack while varying the mounting plate thickness. For this model, the mounting plate is flexure mounted at 3 points (pseudo-kinematic) and subjected to gravity normal to the mirrors. The image performance was found to reach a steady state when the mounting plate reached ~8mm thickness, see Figure 2-11.

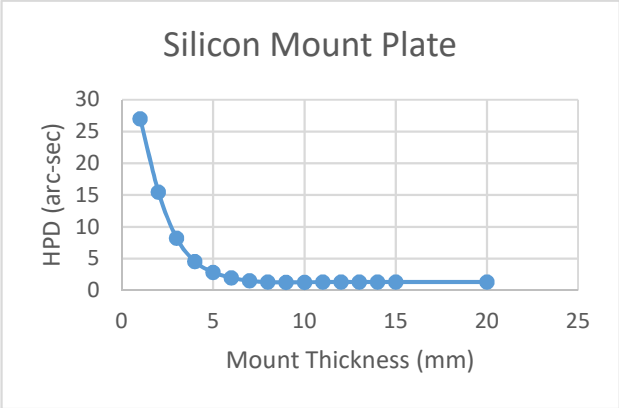

Figure 2-11 Image performance of module as a function of mounting plate thickness

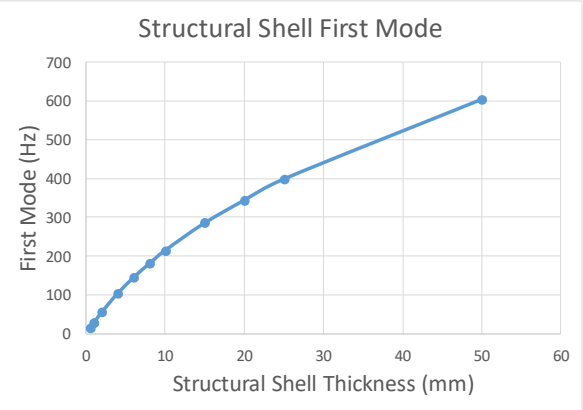

Figure 2-12 Large structural shell modal characteristics as a function of thickness

A similar procedure was conducted on the thickness of a structural shell for a meta-shell. Using mirror stress levels and image quality as the main indicator, again a thickness of >8mm was found to be sufficient for a ~300mm diameter structural shell. Scaling of this data to larger meta-shells was considered insufficient, so an additional study was performed on the largest meta-shell suggested to date, a 2784mm inner diameter shell for the Lynx [6] mission. Stress and image data indicated sufficient thickness at >5mm, but the overall stiffness of the shell was deemed to be of greater concern. Modal analysis was run on the structural shell with the mass of 16 layers of mirrors smeared on, to determine the first mode of the shell. The results are shown in Figure 2-12. If we set a preliminary requirement of 200 Hz first mode, the thickness would need to be 10mm or greater. Given the consistency in the various results, an assumption of 10mm for all structural mounting plates/structural shells has been assumed for various early mission designs.

2.5 Thermal Analysis and Post Material Considerations

Sub-arcsecond X-ray mirror assemblies require excellent thermal stability. Meta-shells are particularly sensitive to radial thermal gradients, as shown in Table 2-3.

Table 2-3 Lynx mirror thermal sensitivities

Lynx Outermost Meta-shell 2.982 meter diameter	
Gradient (1° C)	**HPD (arc-sec)**
bulk	0.31
axial	0.27
radial	3.78
lateral	0.16

Early development of the four point mount was conducted using steel posts for practical considerations (ease of manufacturing). Long term planning led to the consideration of using silicon for the post material. The primary

tradeoff between materials is the combination of manufacturability and thermal performance – silicon is the ideal choice due to its advantageous thermal properties (highly conductive, low thermal expansion) and the thermally homogeneous structure it would create along with the mirrors and structural shells mounted on flexures. To date, manufacturing of silicon posts has proven to be feasible, and all current and future modules use these posts, though a more refined process is still needed. To capture the thermal effects and trade-offs, a trade study was performed using an interlocked meta-shell design.

The tradeoff in thermal performance between materials is a multi-faceted problem, best captured by a detailed STOP (Structural, Thermal, and Optical Performance) analysis, which combines the differences in stiffness, conductivity, and thermal expansion and captures their cumulative effect on mirror performance in a realistic space environment. Temperatures from detailed thermal model that contains spacecraft level thermal control and environmental considerations are mapped onto a structural FE model, and the resulting distortions on the mirror surfaces are ray traced. This analysis was performed on a meta-shell with an inner diameter of 340mm, consisting of 24 layers (16 mirrors per layer) and an outer layer diameter of 450mm. Both the thermal and structural model were run with both silicon and steel spacers, the temperature and optical deformation results are shown in Figure 2-13.

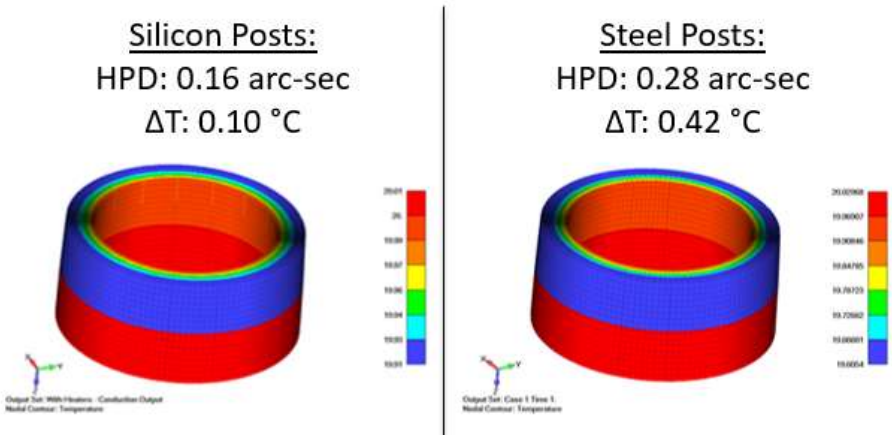

Figure 2-13 STOP results comparison for meta-shells with silicon and steel posts

The net result is a near factor of 2 improvement when switching from steel to silicon spacers, the HPD improves from 0.28 to 0.16 arc-seconds. The most significant effect is due to the higher conductivity in the silicon spacers. The net temperature change over the meta-shell improves by a factor of 4, from 0.42°C to 0.10°C. The CTE is generally considered more critical, but in this case the temperature gradients are so small, and posts so short, that a change of CTE when applied to the same temperature map results in near identical optical distortion. It should be cautioned that this fact does not remain true if there are more substantial thermal gradients, or if the telescope were to operate at a significantly different temperature. To illustrate this, a set of meta-shells ranging from 342mm inner diameter to 1141mm inner diameter, are mounted kinematically along the structural shell to allow free expansion and subjected to a 1°C bulk temperature change. The results are summarized in Table 2-4, for silicon and steel posts, as well as aluminum for reference.

Table 2-4 Meta-shell bulk temperature change sensitivity

Meta-shell	Inner Diameter (mm)	HPD (arc-sec)		
		Silicon	Steel	Aluminum
1	342	0.086	1.204	2.965
2	471	0.115	0.881	2.163
3	615	0.147	1.202	2.870
4	778	0.183	1.340	3.354
5	953	0.222	1.594	3.867
6	1141	0.263	1.718	4.065

It is clear from this data that a bulk temperature change creates a much larger dependence on post material CTE. This suggests that thermal control systems and considerations, both in space and during ground integration, would be much more stringent using steel posts. An additional consideration should be the effects of a radial temperature gradient. The temperature maps from the detailed thermal analysis indicate that the main temperature gradient is in the radial direction. This is mainly due to the fact that temperature control is provided by thin film heaters mounted to the structural shells, and the fact that thermal precollimators are assumed to only have material along the structural shell radii (and posts) so as not to block incoming X-rays from the mirror surfaces. To assess this case, a uniform 1°C radial gradient was mapped onto the meta-shells from the bulk temperature analysis, and analyzed in the same fashion, resulting in the optical deformations summarized in Table 2-5.

Table 2-5 Meta-shell radial temperature gradient sensitivity

Meta-shell	Inner Diameter (mm)	HPD (arc-sec)	
		Silicon	Steel
1	342	1.053	1.852
2	471	0.893	1.573
3	615	1.534	2.433
4	778	2.246	3.143
5	953	2.914	4.098
6	1141	3.727	4.907

This data shows that while the disparity between materials is less dramatic, it still results in substantially less temperature dependence and makes a convincing case for using silicon spacers.

2.6 Flexure Design and Quantity Optimization

Meta-shells are mounted to a spider web shaped carrier structure via blade flexures to form a full optical assembly. The flexure's primary purpose is to isolate the meta-shell from the spider structure to prevent optical deformation from the mismatch of silicon's CTE and the spider (aluminum) when subjected to small temperature changes or gradients. The flexures shown in Figure 2-14 have a bond pad section such that the flexure can be located in place and then bonded to the inside surface of structural shells using injected adhesive. The base section is bolted and pinned to the spider structure. The two thin undercut sections of the flexure allow for radial expansion/contraction of the structural shell as a whole, which is comprised entirely of silicon (other than small amounts of adhesive).

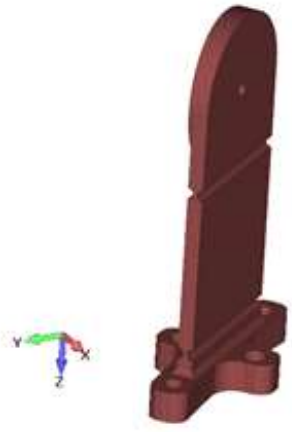

Figure 2-14 Design concept for a meta-shell flexure

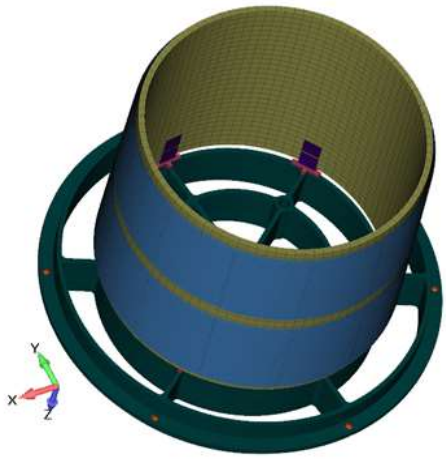

Figure 2-15 Meta-shell used for flexure optimization

Two parameters relating to the flexures have been optimized: the quantity applied to a meta-shell and the thickness of the flexural section. Flexure quantity was determined by examining the 1-G distortion of a 3 layer (12 mirror pairs

per layer) model of a ~300mm diameter shell, shown in Figure 2-15. Both HPD and centroid shift was examined for 5 versions of a shell mounted with between 3 and 12 flexures, at six clockings between 0 and 90 degrees to simulate the change in boundary conditions during the construction of a meta-shell. At 12 flexures, there is uniformity with the 12 mirror pairs, hence the variability in HPD, or range, reduces to zero, and the 1.09 arc-seconds HPD is equivalent to a shell that is fully fixed at the bottom edge. A flexure quantity of 6 appears to be the ideal trade-off, as it minimizes both HPD variation and centroid shift to within 0.02 arc-seconds of fully fixed, while reducing the required number of flexures by half. It also provides a useful and symmetric rule of thumb to other sized meta-shells that the flexure quantity should be half the number of mirror pairs per layer. Results are shown in Table 2-6 and Figure 2-16.

Table 2-6 Distortion summary of a 3 layer meta-shell with variable flexure quantity

# Mounts	HPD (arc-sec)		Centroid (arc-sec)	
	Average	Range	Average Shift	Range
3	1.351	0.043	0.163	0.012145
4	1.214	0.046	0.072	0.000004
6	1.151	0.013	0.047	0.000003
8	1.099	0.011	0.037	0.000003
12	1.088	0.000	0.029	0.000002

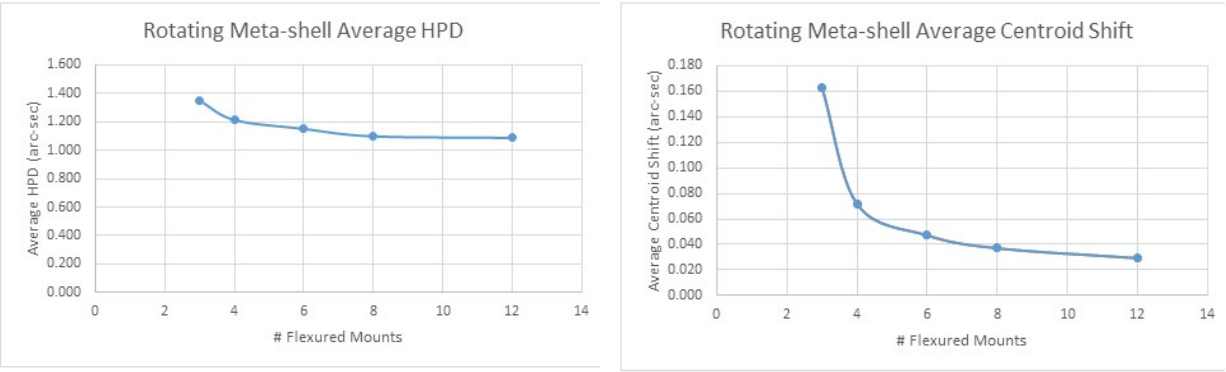

Figure 2-16 Distortion data for 300mm meta-shell by flexure quantity

The flexural section was examined using an identical meta-shell model mounted to an aluminum spider via 6 flexures meshed with plate elements. Both the thin flexural section, and the thicker "bond pad" section were varied while a unit temperature load was applied to the model. If the shell is mounted with purely kinematic boundary conditions at the base (i.e. no flexures/spider) the structure expands uniformly and the resulting distortion is 0.09 arc-seconds HPD of de-focus error. To optimize the bond pad sections, which are desired to be as thin as possible without contributing additional distortion to the shell, the flexure section was set to be extremely thin in the full model to mimic the kinematic case. In that case, the distortion remains around 0.09 arc-seconds until the thickness is increased past ~2mm. The distortion increases with thickness and then plateaus around 0.25 arc-seconds, which can be defined as the effect of the local CTE mismatch of the titanium bond pad on the silicon shell. For the flexure section, a similar set of data was run, this time with the bond pad effectively rigid, with the goal being to determine the maximum thickness the flexural section could be before impacting distortion (increased thickness reduces possible stress issues). As expected, this model showed that a minimal distortion of 0.25 arc-seconds was achieved for very thin sections, equivalent to the local distortion effects previously determined. The relationship between thickness and distortion is shown in Figure 2-17, where the distortion is steady to about 0.5mm thickness, before a small dip at 1.0mm and a sharp increase thereafter. It is therefore recommended that the flexure design contain a flexural section set to 0.5mm and a bond pad section set to 2.0mm.

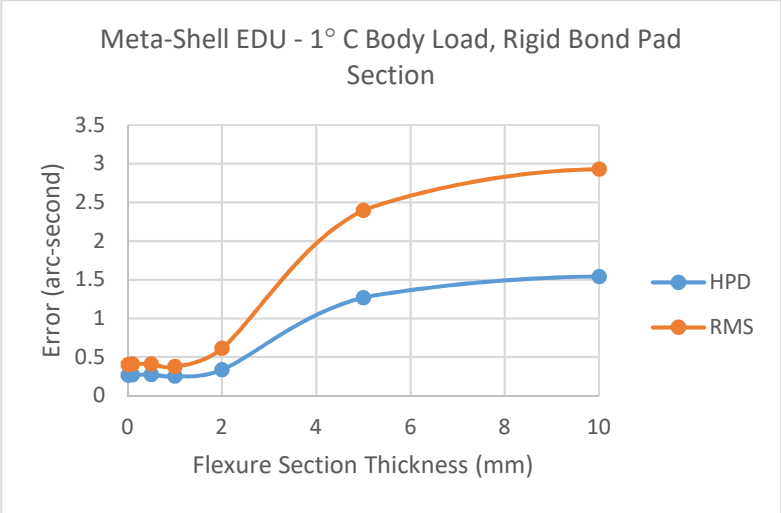

Figure 2-17 Temperature sensitivity of 300mm meta-shell by flexural section thickness

2.7 Survivability Studies and Methods

There have been three detailed efforts at examining the structural integrity of meta-shell designs conducted for an Engineering Design Unit (EDU), the MIDEX level STAR-X [7], and the Lynx decadal submission. These three designs span the full range of possible optical designs: a small 3 layer meta-shell (EDU); a 1.3 meter diameter telescope containing 6 meta-shells (STAR-X); and a 3.0 meter diameter telescope containing 12 meta-shells (Lynx). For STAR-X and the EDU, a static load of 12.3G's axial and 3.4G's lateral was applied. Loads were based on International X-ray Observatory (IXO) Coupled Loads Analysis (CLA) results with a Model Uncertainty Factor (MUF) of 2.0 applied [8]. Resulting stress margins are shown in Table 2-7 and Table 2-8 respectively.

Table 2-7 STAR-X structural analysis results summary

Component	Material	Materail Allowable (MPa)		Peak Stress (MPa)		Factor of Safety		Margin of Safety	
		Ultimate	Yield	Principal	Von Mises	Ultimate	Yield	Ultimate	Yield
Mirrors	Single Crystal Silicon	σ_0=152.5		3.91	3.40	3.0		Weibull Margin = +0.12	
Structural Cylinders	Poly-Silicon	m=8.7		7.72	8.39	3.0		Weibull Margin = +0.58	
Flexures	Titanium	950	880	117.45	103.80	1.4	1.2	+4.78	+6.06
Spider	Al 6061-T6	289	241	28.96	28.20	1.4	1.2	+6.13	+6.12
TPC	G10	448	262	3.78	4.28	1.4	1.2	+83.57	+50.02
Interface Ring	Al 6061-T6	289	241	51.00	48.40	1.4	1.2	+3.05	+3.15
Metering Tube	M55J/954	276	N/A	50.83	44.07	2.0		+1.71	

Table 2-8 Engineering Design Unit (EDU) stress results summary

Component	Material	Material Allowable (MPa)		Peak Stress (MPa)		Factor of Safety		Margin of Safety	
		Ultimate	Yield	Principal	Von Mises	Ultimate	Yield	Ultimate	Yield
Mirrors	SCSi	σ_0=152.5		0.892	0.778	3.0		Weibull Margin = 5.54	
Structural Cylinder	SCSi	m=8.7		1.343	1.431	3.0		Weibull Margin = 3.07	
Flexures	Ti-6Al-4V	950	880	83.487	77.679	1.4	1.2	+7.13	+8.44
Spider	Al 6061-T651	290	241	12.793	11.430	1.4	1.2	+15.19	+16.57

Stress results for the silicon mirrors and structural cylinders are derived using a statistical approach and Weibull [9] statistics developed from 4 point bend tests of single crystal silicon, see section 3.1. The principal stresses and elemental areas of all elements in the FE models (σ_i and A_i respectively) are combined with the Weibull statistics (m, σ_0 and A_0) to calculate failure probabilities of each element, and a cumulative probability of survival (P_s) of the entire assembly:

$$P_s = \prod e^{\frac{-A_i}{A_0}\left(\frac{\sigma_i}{\sigma_0}\right)^m} = e^{\Sigma\frac{-A_i}{A_0}\left(\frac{\sigma_i}{\sigma_0}\right)^m}$$

A scale factor C is then calculated that determines what the input load can be scaled by to reach the minimum required probability (P_{min}):

$$C = \left(\frac{\ln P_{min}}{\ln P_s}\right)^{\frac{1}{m}}$$

In this case we selected a requirement of 1 in 10,000 (0.9998 reliability factor when applied separately to mirrors and structural cylinders) and the margin of safety is C-1. A safety factor of 3.0 is applied to the characteristic strength in accordance with NASA standards [10], in addition to a 0.69 knockdown factor to account for variability of strength in different crystal orientations (0.69 is minimum ratio between known stiffness values in different orientations). Joint margins were also calculated, and were all found to be high.

A purely statistical approach would prove difficult with an assembly the size of Lynx due to the large number of mirrors (37,492) as the probability of failure increases with mirror surface area. An alternate approach was therefore developed using a proof test requirement. To develop the proof test loads, a dynamic analysis was performed on a FE model of the Lynx Mirror Assembly (MA) and a rigidly mounted single mirror, both with analytical force limiting applied [11]. Since bond strength is not critical for a single mirror, the proof test could be achieved by using an easily de-bonded adhesive to temporarily bond the mirror at its four mounting points to a temporary fixture, and then subject it to sine burst loads in two directions:

- Axial (mirror lateral) = 36.7 G's – 3-sigma value of force limited GEVS [12] workmanship on Lynx MA, innermost mirror
- Radial (mirror normal) = 87.6 G's – 3-sigma value of force limited GEVS workmanship on single rigidly mounted mirror

In this case, the Weibull statistics of silicon are still used to calculate a predicted fail rate for the mirrors:

$$P_f = 1 - \prod e^{\frac{-A_i}{A_0}\left(\frac{\sigma_i}{\sigma_0}\right)^m}$$

Stress results from a single mirror model (max stress = 18.4 MPa) and the defined proof loads lead to failure probability, or scrap rate, of 1 in 994, when including a safety factor of 3. Applying that rate to the quantity of mirrors in the Lynx design leads to an estimate of 38 mirror failures during fabrication, well within acceptable levels for full scale mirror production. In a modular meta-shell design, this method could be used to instead apply the proof testing at the modular level, significantly reducing the overall resources needed to be allocated to testing. The cost would be possible failures at the modular level, but given that each set of modules in a meta-shell would contain spares this risk would be manageable.

An additional area of concern for Lynx given the large meta-shells in the design is the strength of the bonded joints at the four posts, specifically at the innermost bonds that are most highly loaded. For these bonded joints, an interaction margin was calculated:

$$MS_{interaction} = \frac{1}{\left(\frac{\sigma_s}{F_s}\right)^{n_s} + \left(\frac{\sigma_t}{F_t}\right)^{n_t}} - 1$$

Where σ_s/σ_t are applied shear/tensile stresses, F_s/F_t are allowable shear/tensile stresses after applied safety factor, and n_s/n_t are interaction coefficients based on coupon testing. For this analysis, values of 45.0 MPa tensile and 27.6 MPa shear are used, corresponding to specification sheet values for Hysol 9313 and a safety factor of 2.0 is applied [10], while linear interaction coefficients are used for conservatism since there is no supporting test data. Each of the 12 meta-shells in the Lynx design was analyzed as a separate structure, and quasi-static Mass Acceleration Curve (MAC) factors were derived based on their masses and data for the Delta IV launch vehicle. An iterative optimization process was then conducted on the diameters of the posts by grouping the posts into 5 sections radially thru the meta-shell. The process started with a nominal design using 4mm posts throughout; each grouping in the meta-shell was then increased/reduced until a near zero positive margin was reached. Results of the process are shown in Table 2-9. The optimization was conducted on the 5 meta-shells highlighted in the table while interpolation was used to determine sizes for the other 7 meta-shells.

Table 2-9 Lynx meta-shell post optimization

Meta-shell	Inner Radius (mm)	# Mirror Layers	Mass (kg)	MAC for Atlas V/Delta IV (G's)	Post Diameter (mm) by Region					Effective Area (m^2)		
					First	Second	Third	Fourth	Fifth	Prescription	Nominal	Tapered
1	126	75	31.3	19.8	9.5	8.0	6.3	4.2	2.4	0.036	0.032	0.031
2	240	61	44.5	18.1	8.8	7.3	5.6	3.7	2.3	0.071	0.065	0.063
3	354	51	54.8	16.4	8.1	6.6	5.0	3.2	2.2	0.108	0.099	0.097
4	468	44	63.7	15.9	7.7	6.2	4.7	3.0	2.2	0.142	0.128	0.126
5	582	39	72.0	15.3	7.4	5.9	4.3	2.8	2.1	0.174	0.158	0.156
6	696	35	79.6	14.8	7.0	5.5	4.0	2.6	2.1	0.202	0.184	0.183
7	810	31	85.3	14.3	6.6	5.1	3.8	2.6	2.2	0.220	0.201	0.200
8	924	28	91.2	13.8	6.2	4.8	3.5	2.5	2.3	0.237	0.216	0.216
9	1039	26	97.9	13.3	5.8	4.4	3.3	2.5	2.4	0.253	0.229	0.231
10	1153	24	103.7	13.3	5.6	4.3	3.2	2.6	2.5	0.261	0.238	0.239
11	1267	22	108.7	12.9	5.5	4.1	3.1	2.6	2.5	0.262	0.238	0.240
12	1381	21	115.5	12.9	5.3	4.0	3.0	2.7	2.6	0.268	0.244	0.246
									Total:	*2.234*	*2.032*	*2.028*

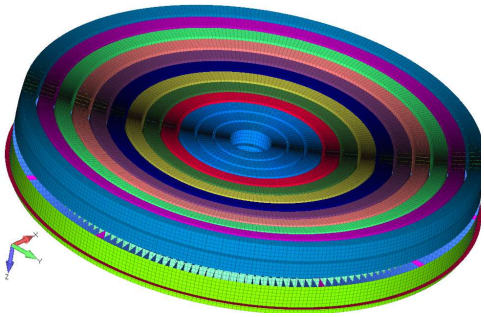

Figure 2-18 Lynx MA FEM

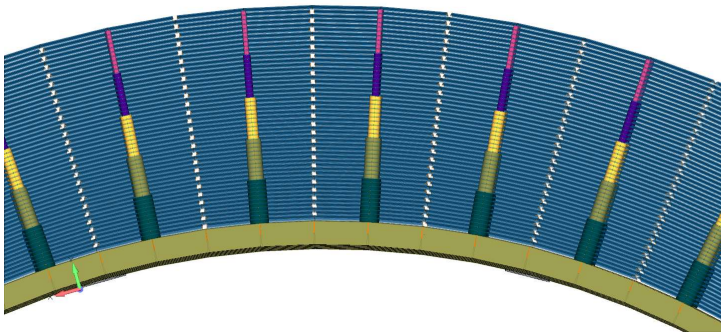

Figure 2-19 Proifle of post optimization result

The main areas of focus for future efforts were identified to be improving the characterization of the silicon mirror material and refining/improving the methods used for determining the strength of the mirror/post bonded joints.

3. STRUCTURAL TESTING

Detailed testing is a necessity for informing the analytical methods used for launch survivability of such a delicate and precise structure, as well as the simulated/calculated error effects calculated for different items of the optical error budget.

3.1 Silicon Material Strength

Characterizing the strength of brittle materials such as silicon is a challenging task. The accepted method for such a task is a 4 point bend test [13]. This test uses rollers and an axial load to generate a pure and constant bending stress on the bottom surface of bar samples, as shown in Figure 3-1. Most samples fracture in the central region, such as in Figure 3-2, but due to occasional existence of larger surface flaws some failures do occur outside the rollers, and these samples must be discarded.

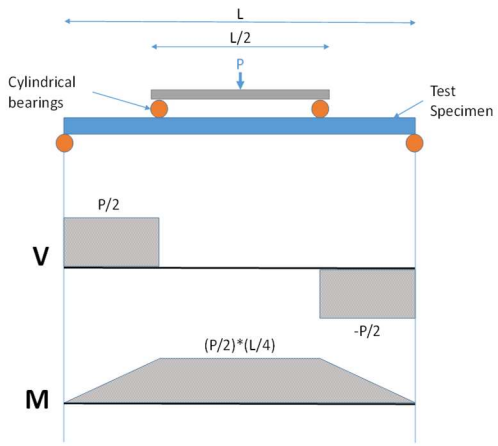

Figure 3-1 Four point bend test

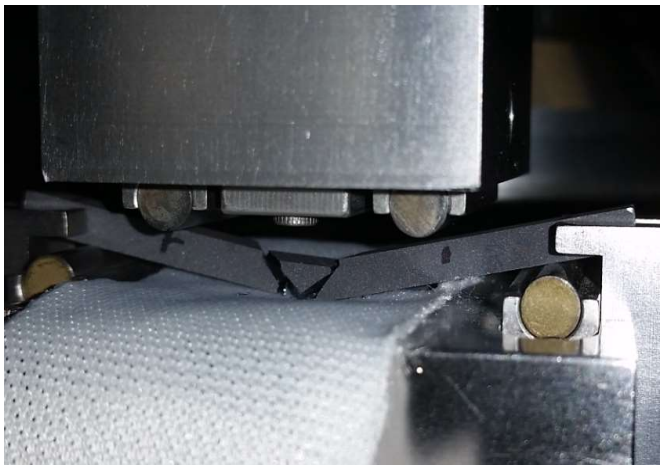

Figure 3-2 Silicon test bar subjected to four point bend test

The resulting data of 30 test samples are plotted in Figure 3-3 and Figure 3-4, and can be used to generate the Weibull statistics that are used for analysis such as that described previously in 2.7. The probability of failure, P_f, is calculated for each specimen by ranking (n) the failure stresses in ascending order from 1 to N, where N is the total number of samples (in this case 30):

$$P_f = \frac{n}{N+1}$$

The Weibull parameters, m and σ_0, are determined using the linear fit of the log-log plot shown in Figure 3-3. The Weibull modulus, m, is equal to the slope of the linear fit. The characteristic strength, σ_0, is the value such that:

$$\ln\left(\ln\frac{1}{1-P_f}\right) = 0 \implies \sigma_0 = e^{\frac{-b}{m}}$$

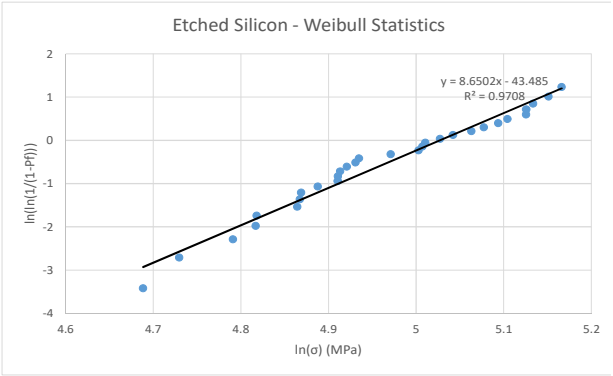

Figure 3-3 Silicon bend bars plotted for Weibull statistics

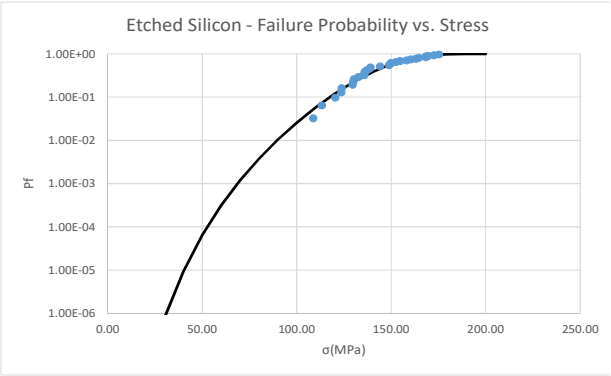

Figure 3-4 Silicon bend bars as a function of failure probability

These samples were cut using wire EDM and etched in an HNA (hydrofluoric, nitric, acetic) acid solution for 30 minutes. To gauge the effects of etching on surface quality, and subsequent material strength, an identical set of samples was tested using un-etched silicon bars. The resulting Weibull parameters are shown in Table 3-1.

Table 3-1 Silicon four point bend test results

Condition	Weibull Parameters		Average (MPa)	Standard Deviation (MPa)
	σ_0 (Mpa)	m		
Un-etched	66.0	24.9	64.6	2.8
Etched 30 Mins	152.5	8.7	144.5	18.3

3.2 Random Vibration and Shock

Both random vibration and shock tests were performed on a single silicon mirror, mounted with 4 posts onto a rigid adapter plate and with a mass simulator, representing 24 shells offset by 28mm (STAR-X innermost meta-shell), bonded to its back surface.

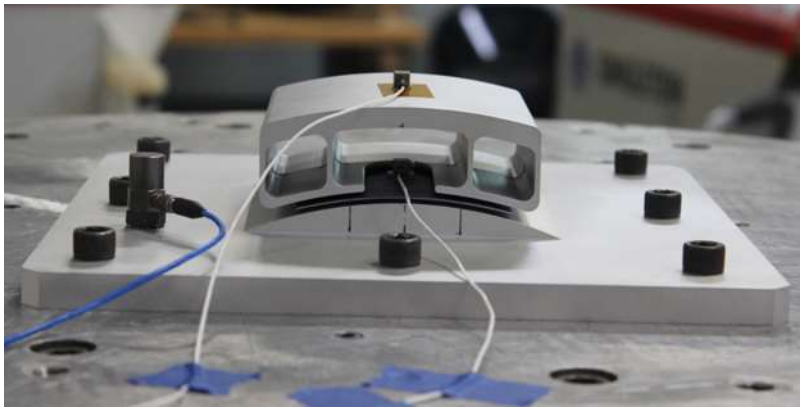

Figure 3-5 Vibration test article

The mirror was subjected to a notched GEVS [12] minimum workmanship level in the radial (X) and axial (Z) directions. In the X direction, a total input of 5.25 GRMS was achieved, producing a response in the mirror accelerometer of 11.6 GRMS. In the Z direction, a +3dB input of 8.84 GRMS, producing a response of 12.9 GRMS.

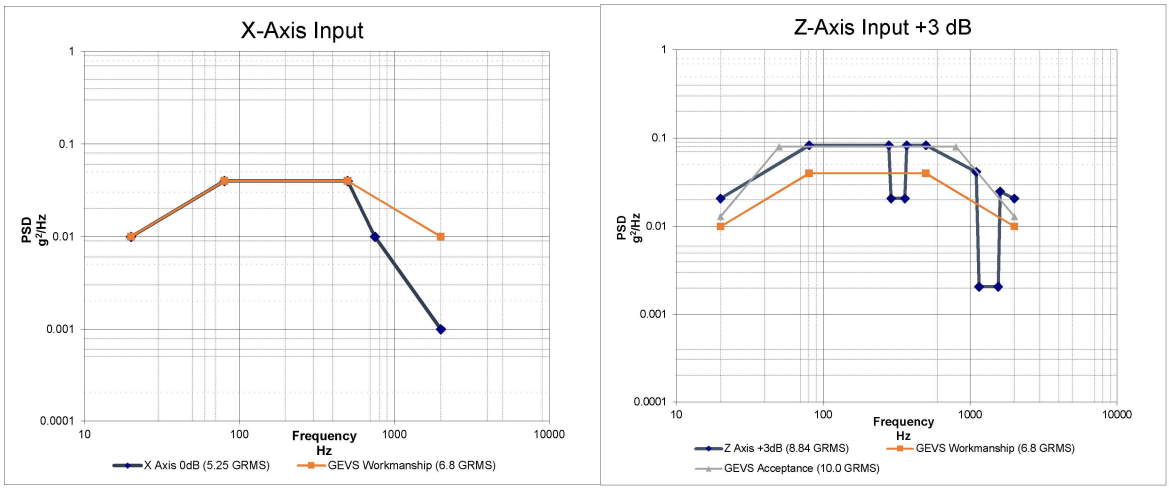

Figure 3-6 Random vibration test inputs

An input Shock Response Spectrum (SRS) curve was developed based on STAR-X requirements, with knockdown factors based on IXO analysis [14]. The shaker table system used for the test was limited to approximately 50% of this input, as such the peak shock input was 210 G's SRS. Pre and Post sine sweeps show that the mirror and bonds were fully intact, though no pre/post optical test was performed.

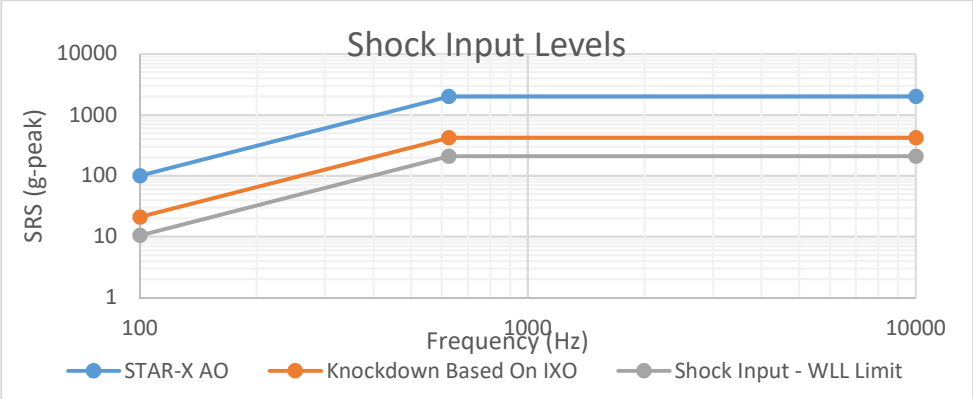

Figure 3-7 NGXO shock test input

3.3 Planned Tests

The tests described in the previous section are preliminary, indeed much work is needed in the near future before the technology is spaceflight qualified. This section describes in brief a summary of the testing work that is planned for the next 2 years.

The large amount of adhesive combined with the precise nature of the optics, requires careful thermal testing to verify that no unforeseen effects are observed. Bonded optics will be subjected to standard thermal vacuum test to confirm that the adhesive bonds are not distorted by the temperature range and vacuum environment that they will see for the duration of mission life in space. The use of spaceflight qualified adhesives and stability of single crystal silicon give us great confidence that no major issues will arise from this testing.

The mirror proof testing concept described in section 2.7 will be implemented and tested on a few representative mirrors. The concept would include simple mounting at 4 points of a mirror to a rigid base, which is then bolted to a vibration table and subjected to quasi-static sine burst loads in all 3 directions.

Additional material strength characterization tests, similar to section 3.1, will also be performed. Initial tests were performed as a pathfinder on silicon bars cut with wire EDM. The surface quality of these samples is no longer a quality representation of the silicon mirrors. Currently the back surface is cut using a band saw, and then etched with an HNA solution notably different than that used for the previous set of bend bars. In addition, the mirror edges are trimmed, then treated and etched again. As this procedure is developed further, additional strength testing should be performed on representative surfaces, and possibly mirror fold tests should be performed to further understand the strength characteristics of the mirror edges, as flaws and crack growth is more likely to occur here.

The random vibration and shock tests detailed in section 3.2 will also be repeated. The goal of the new tests will be to further qualify the bonds of the optics with pre and post test X-ray full illumination testing. This will be crucial to showing that the delicate bonds will maintain X-ray performance after launch. A more accurate, flexure mount design will also be implemented to better simulate possible launch environments and eliminate the need for high frequency notching of the inputs.

The final set of upcoming work will be to repeat these tests with a representative module. Again the goal will be to show that a flight-like article can withstand the rigors of launch, and still maintain X-ray performance. In addition to random vibration, shock, and thermal vacuum, a sine vibration input and sine burst input will also be applied. The module design will be a demonstrator for the OGRE [15] mission, and environmental specifications will therefore attempt to match the input from a sounding rocket.

4. CONCLUSIONS

Silicon X-ray optics are a rapidly progressing technology. This paper has documented the analytical methods that have been employed to date to further improve the theoretical prospects as well as the viability of the technology. Many parameters have been optimized, while potential impacts of larger level assemblies that cannot yet be constructed have been assessed to guide some of the NGXO team's decision making process and priorities.

REFERENCES

[1] Zhang, W. W., et al., "Next-generation astronomical X-ray optics: high-resolution, lightweight, and low-cost," SPIE Proc, Vol. 11119-6, these proceedings, (2019).

[2] Riveros, R.E., et al., "Fabrication of mono-crystalline silicon mirrors for X-ray telescopes," SPIE Proc, Vol 11119-7, these proceedings, (2019).

[3] Biskach, M.P., et al., "Manufacturing of high-resolution and lightweight monocrystalline silicon X-ray optics at scale," SPIE Proc, Vol 11119-8, these proceedings, (2019).

[4] Chan, K. W., et al., "Recent advances in the alignment of silicon mirrors for high-resolution X-ray optics," SPIE Proc, Vol 11119-10, these proceedings, (2019).

[5] Chan, K. W., et al., "Kinematic alignment and bonding of silicon mirrors for high-resolution astronomical X-ray optics," SPIE Proc, Vol 10399, p. 103990U, (2017).

[6] Gaskin, J. A., et al., "The Lynx X-ray Observatory: concept study overview and status," SPIE Proc, Vol 10699, p. 106990N, (2018).

[7] McClelland, R. S., "The STAR-X X-ray Telescope Assembly (XTA)," SPIE Proc, Vol 10399, p. 1039908, (2017).

[8] McClelland, R. S., et al, "Design and Analysis of Modules for Segmented X-ray Optics," SPIE Proc, Vol 8443, p. 84433Y, (2012).

[9] Weibull, W., et al, "A Statistical Distribution Function of Wide Applicability," Journal of Applied Mechanics, Vol. 18, p. 293, (1951).

[10] NASA-STD-5001A, "Structural Design and Test Factors of Safety for Spaceflight Hardware," (2008).

[11] NASA-HDBK-7004C, "Force Limited Vibration Testing," (2012).

[12] GSFC-STD-7000A, "General Environmental Verification Standard (GEVS)," (2013).

[13] ASTM-C1161-02c, "Standard Test Method for Flexural Strength of Advanced Ceramics at Ambient Temperature," (2003).

[14] McClelland, R. S., et al, "Design and Analysis of the International X-Ray Observatory Mirror Modules," SPIE Proc, Vol 7732, p. 773247, (2010).

[15] Tutt, J. H., et al., "The Off-plane Grating Rocket Experiment (OGRE) system overview," SPIE Proc, Vol 10699, p. 106996H, (2018).